System identification of rover dynamics: a comparison of three model structures

Christina M. Ivler*, Norma Gowans and Cole Marfise

University of Portland,
Portland, OR, 97217, USA
Email: ivler@up.edu
Email: nagowans@ucdavis.edu
Email: colemarfise@gmail.com
*Corresponding author

Abstract: Dynamic testing of a small instrumented ground vehicle was conducted in order to identify an accurate state-space model for simulation of autonomous vehicles. This paper describes the application of frequency domain system identification to model the yaw/steering response of a small-scale rover. Several model structures of varying levels of complexity were adapted and applied to a small-scale rover: dynamic bicycle model, roll-yaw model and a lumped (based on Taylor series expansion) model. In comparing these three model structures, it was found that the dynamic bicycle model provided a simple model structure with good performance but cannot model roll dynamics. The roll-yaw model gave the most accurate model and better prediction for a range of vehicle speeds but is significantly more complex. Finally, the lumped model gave a highly accurate model at the identified speed condition; however, it cannot be accurately extrapolated to other speeds.

Keywords: system identification; rover; steering dynamics; bicycle model; frequency domain methods; frequency sweeps; roll-yaw model; ground vehicle; coherence weighted; composite windowing; identification of inertia.

Reference to this paper should be made as follows: Ivler, C.M., Gowans, N. and Marfise, C. (2022) 'System identification of rover dynamics: a comparison of three model structures', *Int. J. Modelling, Identification and Control*, Vol. 40, No. 1, pp.70–83.

Biographical notes: Christina M. Ivler is an Assistant Professor of Mechanical Engineering at the University of Portland. Prior to her current position, she worked for 13 years as a researcher/Engineer for the US Army Aviation Development Directorate (ADD) at Moffett Field, CA. She received her Bachelor and Master's degrees from the UC Davis and PhD from Stanford University. Her research interests are in the area of system identification, flight control design, control allocation and handling qualities for UAS and rotorcraft.

Norma Gowans is a Doctoral student in Mechanical and Aerospace Engineering working as a graduate student researcher at the University of California Davis. Her research interests include control, system identification and dynamics. The year prior to her current position, she worked as an associate researcher at the US Army Aviation Development Directorate. She received her BS degree from the University of Portland as well as conducted research there with Dr. Christina Ivler.

Cole Marfise graduated from the University of Portland in 2020 with a BS in Mechanical Engineering. During his time at the university, he worked as an undergraduate researcher for Dr. Christina Ivler. He currently works for the US Army Corps of Engineers, Portland District, as a Mechanical Design Engineer.

1 Introduction

System identification techniques, in which dynamic models are extracted from measured data, are widely established in respect to air-based vehicles, such as helicopters and fixed-wing aircraft (Tischler and Remple, 2012); however, they are not as prevalent in automotive and rover applications. Frequency domain system identification is widely used to provide highly accurate models for development of control algorithms for unmanned aerial systems (Ivler and Tischler, 2013). In contrast, the development of control algorithms for autonomous ground vehicles typically uses very simple models, many of which are kinematic and do not consider the dynamics of the vehicle at all (Petrov and Nashashibi, 2014; Wan et al., 2019; Alcala et al., 2018). Even in the case that vehicle dynamics are considered, typically in the form of a simple bicycle model, there is rarely validation of the fidelity of the model prior to conducting studies of the control algorithms (Zainal et al., 2017; Zhao et al., 2012; Schildbach and

Borrelli, 2015). There are a few studies that consider model fidelity (Kong et al., 2015, 2014; Tagne et al., 2013; Laws et al., 2006), but little consensus among them as to which model structure is best. The reason for lack of focus on model fidelity of autonomous ground vehicles as compared to autonomous air vehicles may be that the stakes are typically much lower for ground vehicles in terms of the consequences of control instability. Still, even for ground vehicles, the development of accurate models that can better predict vehicle behaviour in simulation will result in less testing and less required tuning of the control algorithms that guide the ground vehicle. This will ultimately reduce costs associated with development of autonomous ground vehicles, as seen for unmanned aerial vehicles (Theodore et al., 2003).

Understanding the ground vehicle modelling process begins with examining previous vehicle dynamics research. A team of researchers at Stanford University have designed a P1 steer-by-wire vehicle, which allows for accurate data collection and vehicle control. It has been found that when accurate and consistent data is obtained, especially at lower frequency inputs, frequency domain modelling is an accurate and trustworthy method of analysis (Laws et al., 2006). Autonomous vehicle modelling research at UC Berkeley has shown the benefits of using a kinematic model and dynamic bicycle model for simulation of steering and tyre control. The simplicity of these models gives a reasonable model for the vehicle under certain conditions. Of the two models, the dynamic bicycle is preferred (Kong et al., 2015). Research at Carnegie Mellon emphasises the importance of using the dynamic bicycle model to approximate vehicle dynamics for tracking at road speeds, as compared to geometric or kinematic models, which are more appropriate for parking lot driving (Sinder, 2009). Aside from the work at Stanford in Laws et al. (2006), frequency domain system identification methods have not been widely applied to autonomous ground vehicles, despite its direct applicability to control stability analysis (Emami-Naeini et al., 2019), and popularity in aerial vehicle modelling (Ivler and Tischler, 2013).

To increase performance and control robustness of a ground vehicle, accurate dynamic responses from steering inputs need to be modelled and understood. System identification can fill this role by extracting dynamic models from measured data collected onboard the vehicle. This paper will use frequency domain system to identify lateral dynamics steering (linear) models and compare their relative predicative accuracy to the true (measured) vehicle responses. The three models selected for comparison are the dynamic bicycle model, the roll-yaw model, and the lumped model. It should be noted that these models are all linear state-space models, as such there are negligible differences in computation efficiency of simulation of these models.

This work contributes new information about the accuracy of three common model structures for small ground vehicles in the frequency domain. Despite the common usage of these models for autonomous control studies, model accuracy in the frequency domain for ground vehicles is overlooked (Zainal et al., 2017; Zhao et al., 2012; Schildbach and Borrelli, 2015; Farag, 2020; Shao et al., 2019) despite this being an important parameter for robust control system design (Emami-Naeini et al., 2019). This work is novel in the application of use of the frequency sweep method for data collection, the frequency domain-based identification technique which has only previously been applied to aircraft, and evaluation of model accuracy and trade-offs in the frequency domain. These results have important impact with regards to developing models for future use in autonomous systems, where model accuracy affects the ability to accurately design and simulate performance. Herein, the authors provide new guidance on when each model structure is best utilised.

2 Background

2.1 Vehicle and instrumentation

The system identification process was performed on a small-scale ground rover, known as the University of Portland (UP) rover, shown in Figure 1(a). The UP rover was built on a 1/10 Traxxas Slash 2WD chassis. The vehicle is powered by a Titan 12 brushless motor. The chassis was fitted with a mounting board holding a Pixhawk 2.1, which combines sensors, instrumentation, and control system into a single package. The Pixhawk control system takes in commands from the radio or ground station (depending on if it is in manual or autonomous mode), and provides the appropriate motor and steering commands to the electronic speed controller (ESC) and steering servo, respectively. The Pixhawk was also used for data acquisition in this research as it contains dual inertial measurement units (with three-axis accelerometers and rate gyros), GPS and barometric altitude. The Pixhawk also logs the control input signals to the ESC and steering servo, which are needed for system identification.

2.2 Mass moment of inertia

An inertia swing test of the Traxxas Slash was conducted to calculate the mass moment of inertia. The inertia values were calculated via experimentation for use later in model validation. The experimental test setup and equations are defined in Figure 1(b) and equations (1)–(2), per Koken (2017). First, the configuration is tested as a simple pendulum, to determine if the resulting calculation of gravity in equation (1) is close to the known value of 9.81 m/s^2. If it is sufficiently close, then the mass moment of inertia about the axis shown in the dashed black line can be determined with equation (2) via measurement of the period of swing about the dashed axis.

$$g = \frac{4\pi^2 h}{T^2} \tag{1}$$

$$I = \frac{mgd^2T^2}{16\pi^2 h} \tag{2}$$

The period of the swing oscillation T after perturbation, around the axis of interest is measured as a key input to equation (2). The calculated mass moment of inertia for the Traxxas Slash platform about the z-body axis, oriented upward (away from the ground) on the rover, was I_z = 0.064 kg-m^2. Similarly, the mass moment of inertia about the x-axis, oriented forward (out the nose) of the rover, was I_x = 0.008 kg-m^2.

Figure 1 UP setup for rover dynamics experiments, (a) UP rover (b) swing test for UP rover (see online version for colours)

(a)

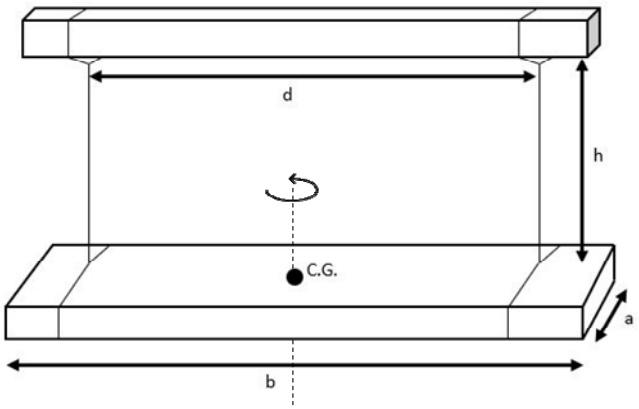

(b)

3 Frequency domain system identification method

System identification is a procedure for efficiently extracting dynamic models from measured control inputs and resulting output response of a mechanical system. The system identification methodology used here is the frequency domain method as described in Tischler and Remple (2012) and Ivler and Tischler (2013). This system identification methodology has five main steps: data collection, frequency response identification, state-space model fitting to the MIMO frequency response database, model structure determination and time domain verification. The methodology is well suited to identification of dynamic characteristics due to its insensitivity to uncorrelated output noise (which produces a bias in time-domain methods), and its ability to identify unstable dynamics (which is also difficult in the time domain due to divergence). The key steps in the frequency domain system identification process are discussed in the following sections.

3.1 Data collection

Prior to performing the system identification procedure, measured data must be collected on the vehicle of interest. In order to identify a frequency response of the vehicle over the frequency range of interest, the vehicle must be excited accordingly: the first rule of system identification is that you cannot identify what is not in the data. Frequency sweep manoeuvres are designed to provide a robust spectral excitation across the frequency range of interest for system identification. In a frequency sweep, the input is 'swept' in a sine-wave like excitation that increases in frequency over the record. Although many different types of manoeuvres can be used to excite the vehicle across a wide frequency spectra, such as white noise or sum-of-sines, frequency sweeps have been found experimentally to provide good quality frequency responses (Tischler and Remple, 2012). Frequency sweeps have the added benefit that they are easily conducted either manually or automatically. If implemented automatically, the following equations are recommended:

$$\delta_{sweep} = A\sin\left(\theta(t)\right) \tag{3}$$

$$\theta(t) = \int_0^{T_{rec}} \omega(t)dt \tag{4}$$

where the exponential frequency progression is given by (Tischler and Remple, 2012):

$$\omega(t) = \omega_{\min} + 4\left(e^{0.0187t/T_{rec}} - 1\right). \tag{5}$$

3.2 Frequency response identification from measured data

This step identifies input to output frequency response functions from measured data. After data is collected on the vehicle, a Chirp-Z transform calculated from overlapping tapered windows is used to initially transform time-domain data to the frequency-domain. This results in the frequency domain input $X(f)$ and output $Y(f)$. The autospectra for the input and output are calculated (Tischler and Remple, 2012):

$$\begin{aligned} &\text{Input autospectrum:} && G_{xx}(f) = \frac{2}{T}\left|X(f)\right|^2 \\ &\text{Output autospectrum:} && G_{yy}(f) = \frac{2}{T_{win}}\left|Y(f)\right|^2 \\ &\text{Cross-spectrum:} && G_{xy}(f) = \frac{2}{T_{win}}\left[X^*(f)Y(f)\right] \end{aligned} \tag{6}$$

*indicates complex conjugate

The frequency response, which captures the input to output dynamics, can then be determined by:

$$T(f) = \frac{Y}{X}(f) = \frac{G_{xy}(f)}{G_{xx}(f)} \tag{7}$$

The associated coherence function is related to the correlation of the input to output responses, and therefore is a measure of the overall quality and linearity of the frequency response. The coherence function is calculated by:

$$\gamma_{xy}^2(f) = \frac{|G_{xy}(f)|^2}{|G_{xx}(f)||G_{yy}(f)|} \tag{8}$$

Generally speaking, over the frequency range that $\gamma_{xy}^2(f) > 0.6$ indicates where the frequency response $T(f)$ is of good quality.

This process is performed for several overlapping window sizes, so that they can later be averaged. The short windows provide more averaging and therefore reduce random error at high frequency. Longer windows better identify a broad dynamic range because they inherently capture a longer period of response. To account for this, the overall frequency range of accuracy is improved by combining a weighted average of multiple windows, in a method known as composite windowing, as described in detail by Tischler and Remple (2012). Once a database of composite frequency responses $T_c(f)$ are calculated, where all input-to-output responses of interested are determined, then a state-space model can be identified to fit these data.

3.3 State space model identification

A state-space model structure is chosen by the user, based on analysis of the frequency responses or known physics of the system. The format of the state-space model is:

$$\boldsymbol{M}\dot{\boldsymbol{x}} = \boldsymbol{F}\boldsymbol{x} + \boldsymbol{G}\boldsymbol{u} \tag{9}$$

$$\boldsymbol{y} = \boldsymbol{H_o}\boldsymbol{x} + \boldsymbol{H_1}\dot{\boldsymbol{x}} \tag{10}$$

The states are defined by the user, as are the parameters in the $\boldsymbol{M}$, $\boldsymbol{F}$ and $\boldsymbol{G}$ matrices. Parameters can be selected as fixed or freed. Known parameters such as gravity constants or mass of the vehicle can be fixed, whereas unknowns such as tyre coefficients, roll centre distance and inertias may be selected as 'free', meaning they will be identified in the system identification process. The $\boldsymbol{H_o}$ and $\boldsymbol{H_1}$ matrices are used to map the model states ($\boldsymbol{x}$) to the measured signals ($\boldsymbol{y}$). A coherence weighted cost function (J) is used to quantify the match between flight data and the state space model. The freed state-space model parameters are optimised to minimise the coherence weighted cost function:

$$J = \sum_{l=1}^{n_{TF}} \left\{ \frac{20}{n_\omega} \sum_{\omega_1}^{\omega_{n_\omega}} W_\gamma \left[W_g \left(|T_c| - |T_m| \right)^2 + W_p \left(\angle T_c - \angle T_m \right)^2 \right] \right\} \tag{11}$$

In the cost function, the composite frequency responses from the measured data T_c are compared to the model transfer functions T_m. n_{TF} represents the number of transfer functions used in the identification and n_ω is the number of frequency points used in the cost function (20 is recommended). $W_\gamma(\omega) = [1.58(1 - e^{-\gamma_{xy}^2})]^2$ is a coherence weighting to ensure the highest quality data is more heavily weighted in the cost function, W_g = 1.0 is the magnitude weighting, and W_p = 0.01745 is the phase weighting. The magnitude and phase weightings were designed to equally weigh the real and imaginary parts of the complex transfer function error (Tischler and Remple, 2012).

3.4 Model structure evaluation

After optimising the model parameters to provide the lowest possible cost function J from equation (11), the next step is to evaluate the uniqueness and reliability of each parameter. Insensitivity is evaluated to determine how sensitive the cost function is to each parameter. The Cramer-Rao bound is a measure of the uniqueness (non-correlation) of each parameter. Both the Cramer-Rao bound CR and insensitivity I are based on the Hessian matrix H for the cost function J with respect to the identified model parameters Θ.

$$H = \begin{bmatrix} \frac{\partial^2 J}{\partial \theta_1^2} & \frac{\partial^2 J}{\partial \theta_1 \partial \theta_2} & \text{A} & \frac{\partial^2 J}{\partial \theta_1 \partial \theta_{n_p}} \\ \frac{\partial^2 J}{\partial \theta_2 \partial \theta_1} & \frac{\partial^2 J}{\partial \theta_2^2} & \text{A} & \frac{\partial^2 J}{\partial \theta_2 \partial \theta_{n_p}} \\ \text{C} & \text{C} & \text{E} & \text{C} \\ \frac{\partial^2 J}{\partial \theta_{n_p} \partial \theta_1} & \frac{\partial^2 J}{\partial \theta_3 \partial \theta_2} & \text{A} & \frac{\partial^2 J}{\partial \theta_{n_p}^2} \end{bmatrix} \tag{12}$$

$$CR_i = 2\sqrt{(H^{-1})ii} \tag{13}$$

$$I_i = \frac{1}{\sqrt{H_{ii}}} \tag{14}$$

It is recommended by Tischler and Remple (2012) that $I \leq 10\%$ and $CR \leq 20\%$ are reasonable goals that provide a reliable model. Parameters that have undesirably large insensitivities and/or Cramer-Rao bounds cannot be accurately determined given the available data and model structure. This means that these parameters can be set to a wide range of values without affecting the cost function, or are highly correlated with another parameter and so cannot be accurately identified with good confidence. These terms are removed from the set of identified parameters in the optimisation by setting them to a fixed value, which is either zero or a best guess of the value. For example, inertias are sometimes highly correlated with other parameters and so must be fixed to an estimated or experimentally obtained value. The model is re-converged after each parameter is removed. This ensures that in the final model, all parameters are sensitive to the cost function and that there are no correlated parameters in the model.

3.5 Time domain verification

Once a model that well fits the frequency data has been determined, the model is verified in the time domain using data that was not previously used in the identification process. This ensures the model is not overly tuned to a single data run, so that the model is not an over-parameterised curve fit but rather captures the true physics. Doublets in each axis are used for verification. The state space model is driven with measured input data, and the model outputs are evaluated against the measured output motion of the vehicle. A cost function is used to measure the match between the model and the flight data.

$$J_{rms} = \left(\frac{1}{n_t n_o} \sum_{i=1}^{n_t} \left(\boldsymbol{y_{data}} - \boldsymbol{y_m} \right)^T \boldsymbol{W} \left(\boldsymbol{y_{data}} - \boldsymbol{y_m} \right) \right)^{\frac{1}{2}} \tag{15}$$

In the cost function, n_t is the number of time points, n_o is the number of output signals compared in the verification, $\boldsymbol{W}$ is user-defined weighting, and $\boldsymbol{y_{data}}$ is an array representing the measured response of the vehicle during the manoeuvre, whereas $\boldsymbol{y_m}$ is an array of the model response of the vehicle (to the measured input signal). A cost function of $J_{rms} < 2.0$ is recommended by Tischler and Remple (2012) for aircraft model validation. A normalised cost function, known as the Thiel inequality coefficient (TIC) is a normalised form of the cost function:

$$TIC = \frac{J_{rms}}{\left(\frac{1}{n_t n_o} \sum_{i=1}^{n_t} \left(y_m \right)^T W \left(y_m \right) \right)^{\frac{1}{2}} + \left(\frac{1}{n_t n_o} \sum_{i=1}^{n_t} \left(y_{data} \right)^T W \left(y_{data} \right) \right)^{\frac{1}{2}}} \tag{16}$$

The *TIC* can be thought of as a normalised error. For aircraft *TIC* < .35 (or 35%) is considered acceptable, but lower is better.

These steps shown in Section 3.1–Section 3.5 are implemented by the CIFER® software in the analyses presented in this paper. The following sections will describe how the frequency domain identification was adapted and applied to the UP rover to extract system identification models.

4 Data collection on the ground rover

Manual frequency sweeps were first executed in this research but were difficult to perfect for inexperienced drivers (the authors of this paper). For this application, automated frequency sweeps were found to be more consistent and produce better-quality frequency responses. In the case of automated sweeps, equations (3)–(5) were used to generate the steering input. For the rover application, the steering frequency sweep parameters that were used are given in Table 1.

The flexibility of the open source Ardupilot Rover software package installed on the Pixhawk proved useful for programming the automated sweeps onto the rover. The sweep parameters were programmed such that they could be updated during testing via the ground station for improved efficiency. Switch 6 on the DX6 controller was programmed to trigger/terminate the frequency sweep. The remote operator would input a constant throttle input to achieve the desired speed, which was easy to implement because the DX6 does not have a spring on the throttle. This type of transmitter is typically used for aerial drones, but its throttle and switches made it useful for this application.

Table 1 Frequency sweep parameters for rover testing

Sweep parameter	*Description*	*Value (s)*
A	Amplitude	±150 μs (PWM)
$\omega_{\min}$	Minimum frequency	0.3 rad/s
$\omega_{\max}$	Maximum frequency	25 rad/s
T_{rec}	Sweep length	55 s

The programmed frequency sweep input with pulse-width-modulation (PWM) amplitude of ±150 μs was input to the steering channel as shown in the upper subplot of Figure 2, and the resulting yaw rate of the rover is shown in the lower subplot. The achieved rover yaw rate is approximately ±40–45 deg/s, until the response rolls off as expected at higher frequencies.

Figure 2 Frequency sweep input and output

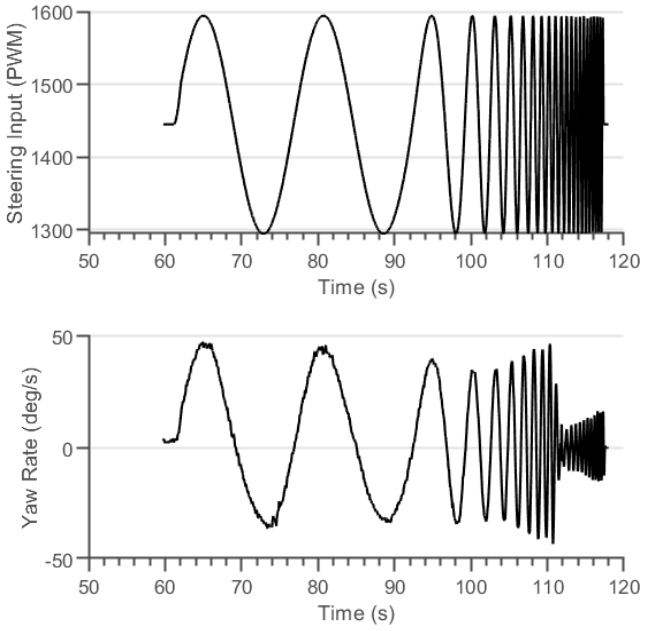

5 Frequency response identification of the rover

After collection of the data, input-to-output frequency responses were identified using the process described earlier. The identified frequency responses are shown in Figure 3. The coherence can be used to gauge the accuracy and quality of each frequency response. High coherence indicates the quality of the frequency response – associated

with linearity and correlation of the input-to-output relationship. The frequency response is the first harmonic (linear) representation of the input to output response and so nonlinearities can degrade coherence. The coherence will also degrade if there is poor signal-to-noise ratio in the sensed output, resulting in poor input-to-output correlation. It is desirable to have coherence of greater than about $\gamma_{xy}^2 \geq 0.6$ for use in state-space modelling. When determining the frequency ranges of each frequency response to use for identification of the state-space model, the range where $\gamma_{xy}^2 \geq 0.6$ is used, although local drops in coherence are sometimes included if the coherence is good on either side of that region. The frequency ranges of acceptable accuracy ultimately used in the state-space system identification (indicating a wide frequency range of accuracy) were: r / δ: 0.2–25 rad/s, a_y / δ: 0.2–25 rad/s, p / δ: 0.6–20 rad/s and $\dot{V}_y^{\circ} / \delta$: 3–25 rad/s.

6 State-space model identification and model structure evaluation

After identifying a set of input-to-output frequency responses, which represent a non-parametric model of the rover, a parametric state-space model can be identified to best fit these data. Herein, three state-space model structures of varying complexity were used to identify parametric models of the rover. As mentioned in the introduction, there is little guidance as to which model structure is most appropriate and very little literature where frequency domain verification of model dynamics was conducted. As such, this study evaluates the accuracy of each of three common model structures to provide insight into the most appropriate modelling method for a rover. The three model structures used were the bicycle model, the roll-yaw model and the lumped model. Each of these model structures are described in the following sections.

6.1 Dynamic bicycle model

Ground vehicles can be modelled using the dynamic bicycle model, which takes advantage of the vehicle's symmetry to lump the two front tyres into a single front tyre model that can steer, and similarly, the two rear tyres are modelled as one lumped rear tyre that does not steer. In this model, only the in-plane yawing motion about the *z*-axis is considered, neglecting the roll and pitch dynamics.

The equations of motion are derived from the centre of gravity, *x*-position, and *y*-position in the inertial frame (Kong et al., 2015). The inertial position coordinates and steering angle in the dynamic bicycle model are defined in Figure 4.

Figure 3 Identified frequency responses at 2.4 m/s, on asphalt, (a) lateral acceleration (m/s^2) to steering input (μs), $\frac{a_y}{\delta}$ (jω) (b) yaw rate (rad/s) to steering input (μs), $\frac{r}{\delta}$ (jω) (c) roll rate (rad/s) to steering input (μs), $\frac{p}{\delta}$ (jω) (d) lateral velocity rate (m/s^2) to steering input (μs), $\frac{\dot{V}_y^{\circ}}{\delta}$ (jω)

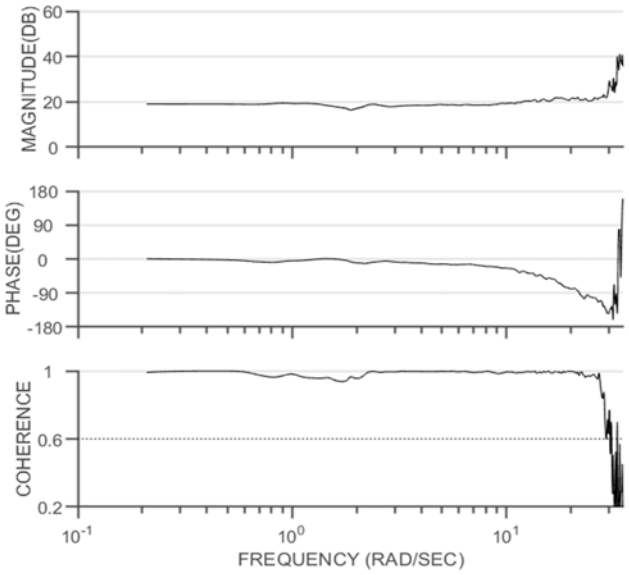

(a)

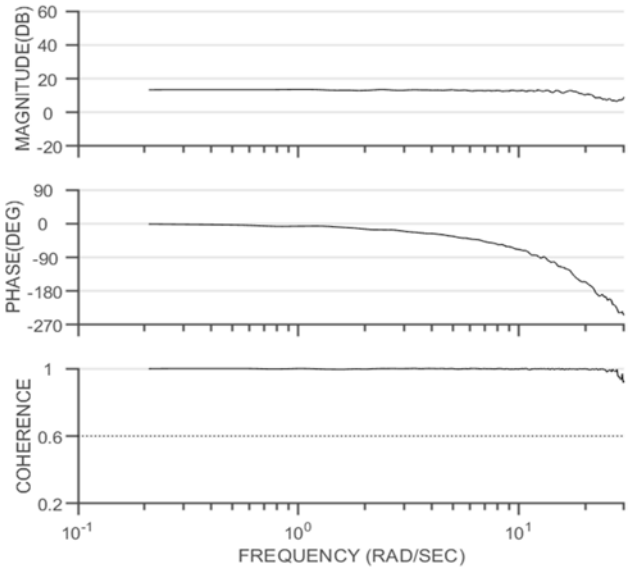

(b)

Figure 3 Identified frequency responses at 2.4 m/s, on asphalt, (a) lateral acceleration (m/s^2) to steering input (μs), $\frac{a_y}{\delta}$ (jω) (b) yaw rate (rad/s) to steering input (μs), $\frac{r}{\delta}$ (jω) (c) roll rate (rad/s) to steering input (μs), $\frac{p}{\delta}$ (jω) (d) lateral velocity rate (m/s^2) to steering input (μs), $\frac{\dot{V}_y}{\delta}$ (jω) (continued)

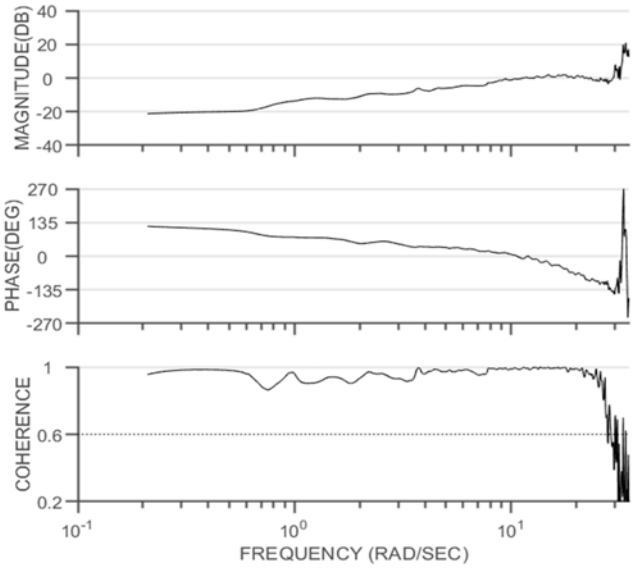

(c)

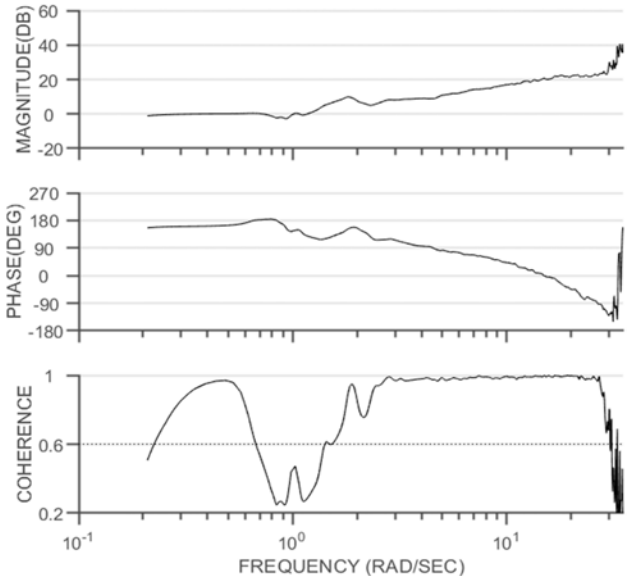

(c)

The equations of motion in the state-space form for the dynamic bicycle model are:

$$\begin{bmatrix} \dot{\beta} \\ \dot{r} \end{bmatrix} = \begin{bmatrix} \frac{-C_o}{mV_x} & \frac{-C_1}{mV_x^2} - 1 \\ \frac{-C_1}{I_z} & \frac{-C_2}{I_z V_x} \end{bmatrix} \begin{bmatrix} \beta \\ r \end{bmatrix} + \begin{bmatrix} \frac{C_{\alpha_f}}{mV_x} \\ \frac{aC_{\alpha_f}}{I_z} \end{bmatrix} \delta(t-\tau) \qquad (17)$$

The states are sideslip, $\beta = V_y / V_x$ and yaw rate r. The forward speed V_x is assumed to be constant. The coefficients are defined as $C_o = C_{\alpha_f} + C_{\alpha_r}$, $C_1 = aC_{\alpha_f} - bC_{\alpha_r}$ and $C_2 = a^2 C_{\alpha_f} + b^2 C_{\alpha_r}$. The front and rear tyre cornering stiffness are C_{α_f} and C_{α_r}, respectively.

Figure 4 Dynamic bicycle model

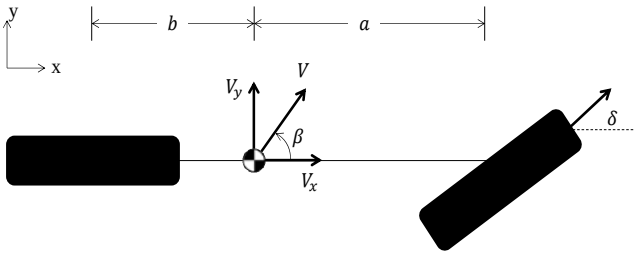

Table 2 shows the final identified model parameters. As shown in Table 2, some parameters in the model were fixed based on known properties of the vehicle during the test, namely the speed, mass, and front/rear distance to the centre of gravity (a and b). Mean forward ground speed V_x was calculated by averaging the Kalman filter estimate of the ground speed during the rover frequency sweeps. Other parameters that are not well known were identified. For the bicycle model structure, only three parameters were identified: mass moment of inertia, tyre cornering stiffness and equivalent time delay. The front and rear tyre stiffness could not be individually identified, as they were highly correlated with one another. Instead, they were constrained to be equal. The front and rear tyres on the rover are identical, so this was a reasonable assumption to make.

Although the inertia was estimated earlier from a swing test, the swing period was measured manually (stop watch) and there was no correction made for drag in the swing test, so the test was imperfect. Generally, vehicle inertia is a source of uncertainty in dynamic modelling and as such the ability to identify mass moments of inertia with system identification is desirable. For these reasons, the inertia was selected as a free parameter in the identification, as opposed to being fixed to the swing test value. Still, the identified value I_{zz} = 0.085 kg m^2 which is within 25% of the swing test value I_{zz} = 0.064 kg m^2, providing confidence in the identification method to determine a reasonable value for mass-moment of inertia.

The cornering stiffness of the tyres were identified as $C_{\alpha_r} = C_{\alpha_f} = 22.6 \pm 0.85$ N/rad (with Cramer-Rao bound of 0.85 or 3.76%). This value is reasonably consistent with Hoblet (2003) which experimentally determined (via test apparatus) the cornering stiffness of five different model car tyres and found them to range from approximately 23 N/rad to 55 N/rad. It should be noted that none of the model car tyres tested in were Hoblet (2003) the exact model used in the study herein, but still provides confidence that the identified value is of the correct order of magnitude.

Table 2 Identified bicycle model

Parameter	*Description*	*Value*	*Free/fixed*	*Cramer-Rao (%)*	*Insensitivity (%)*
a	Distance from front axle to CG	0.33 m	Fixed	-	-
b	Distance from rear axle to CG	0.24 m	Fixed	-	-
m	Mass of rover	2.64 kg	Fixed	-	-
V_x	Forward speed of rover	2.4 m/s	Fixed	-	-
$C_{\alpha_r} = C_{\alpha_f}$	Tyre cornering stiffness	22.6 N/rad	Free	3.76	1.85
I_{zz}	Mass moment of inertia for the z-body axis	0.085 kg m^2	Free	14.4	5.56
τ	Equivalent time delay	0.072 s	Free	7.97	3.04

Table 3 Roll-yaw model parameters

Parameter	*Description*	*Value*	*Free/fixed*	*Cramer-Rao (%)*	*Insensitivity (%)*
a	Distance from front axle to CG	0.33 m	Fixed	-	-
b	Distance from rear axle to CG	0.24 m	Fixed	-	-
m	Mass of rover	2.64 kg	Fixed	-	-
m_s	Sprung mass of rover	2.38 kg	Fixed	-	-
V_x	Forward speed of rover	2.4 m/s	Fixed	-	-
I_{xz}	Cross-product of Inertia	0	Fixed	-	-
I_{xx}	Mass moment of inertia for x-body axis	0.008 kg m^2	Fixed	-	-
h	Height of CG above roll centre	0.06 m	Fixed	-	-
I_{zz}	Mass moment of inertia for the z-body axis	0.056 kg m^2	Free	8.10	3.17
$C_{\alpha_r} = C_{\alpha_f}$	Tyre cornering stiffness	35.34 N/rad	Free	4.42	1.62
k_ϕ	Suspension spring constant	10.4 N/m	Free	3.81	1.82
b_ϕ	Suspension damping constant	0.828 N/(m/s)	Free	8.88	3.91
τ	Equivalent time delay	0.088 s	Free	7.97	3.04

Table 4 Lumped model parameters

Parameter	*Description*	*Value*	*Free/fixed*	*Cramer-Rao (%)*	*Insensitivity (%)*
V_x	Forward speed of rover	2.4 m/s	Fixed	-	-
Y_v	Lateral side force due to lateral velocity	0	Fixed	-	-
Y_p	Lateral side force due to roll rate	1.80	Free	30.2	7.98
Y_r	Lateral side force due to yaw rate	0	Fixed	-	-
Y_ϕ	Lateral side force due to roll angle	0	Fixed	-	-
Y_δ	Lateral side force due to steering angle input	71.5	Free	28.5	3.40
L_v	Rolling moment due to lateral velocity	0	Fixed	-	-
L_p	Rolling moment due to roll rate	–17.5	Free	19.3	2.64
L_r	Rolling moment due to yaw rate	–6.50	Free	16.1	0.652
L_ϕ	Rolling moment due to roll angle	0	Fixed	-	-
L_δ	Rolling moment due to steering angle input	31.1	Free	16.4	0.625
N_v	Yawing moment due to lateral velocity	–1.87	Free	33.0	10.2
N_p	Yawing moment due to roll rate	36.6	Free	15.2	2.19
N_r	Yawing moment due to yaw rate	–9.13	Free	18.0	0.832
N_ϕ	Yawing moment due to roll angle	71.52	Free	28.5	3.4
N_δ	Yawing moment due to steering angle input	32.0	Free	25.7	1.09
τ	Equivalent time delay	0.0711	Free	5.22	1.52

The equivalent time delay τ is used to better capture the effects on the phase of higher-order unmodelled dynamics. A higher order model could capture the same effect via physics. Pure time delays only affect the phase of the transfer function, and do not change the magnitude. It has been found in the aerial vehicle system identification (Ivler and Tischler, 2013) that modelling higher order dynamics as a time delay captures the key effect of the dynamics on the lower frequencies, because the phase of a mode typically affects the dynamics over a wider frequency range than magnitude. The ability to better capture the phase response by using a low order model combined with an equivalent time delay results in better prediction of stability margins and less model complexity (Ivler and Tischler, 2013).

The model costs and plots against the measured data are shown and discussed later, in comparison with the other two model structures, in Table 5 and Table 6, as well as in Figure 6–Figure 7.

Figure 5 Roll-yaw model schematic, (a) top view (b) back view

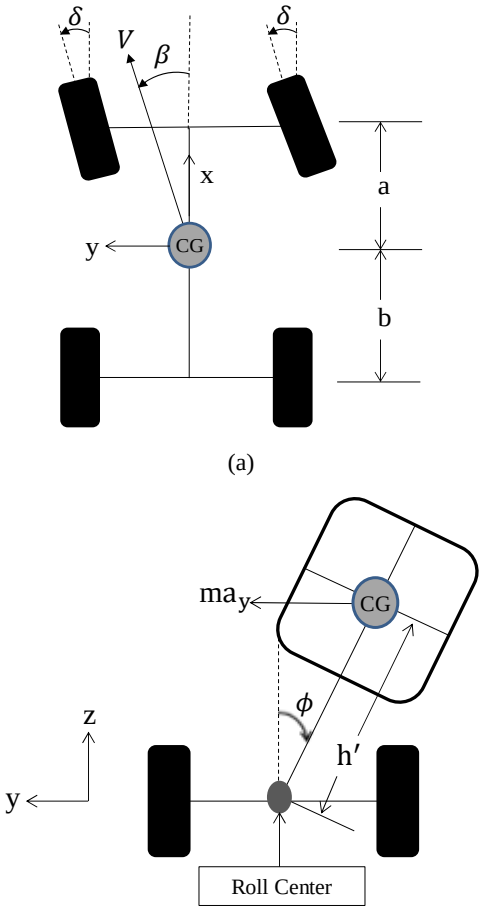

6.2 Roll-yaw model

The roll-yaw model is a more complex model that allows for rolling motion about the *x*-body axis, in addition to yawing motion about the *z*-axis. Key model geometry and physical parameters can be observed in Figure 5. The roll analysis is performed by moment balance about the roll centre of the vehicle, as illustrated in Figure 5(b). The roll and yaw motion are coupled in this model structure. The tyres are assumed to have symmetric slip angles across the left and right sides, and so are lumped in the dynamic equations into total front tyre and rear tyre forces, like the bicycle model.

Figure 6 Frequency domain validation of models, 2.1 m/s on concrete, (a) yaw rate (rad/s) to steering input (μs), $\frac{r}{\delta}(j\omega)$ (b) roll-rate (rad/s) to steering input (μs), $\frac{p}{\delta}(j\omega)$ (c) body-axis velocity rate (m/s^2) to steering input (μs), $\frac{v_s}{\delta}(j\omega)$ (d) lateral acceleration (m/s^2) to steering input (μs), $\frac{a_y}{\delta}(j\omega)$

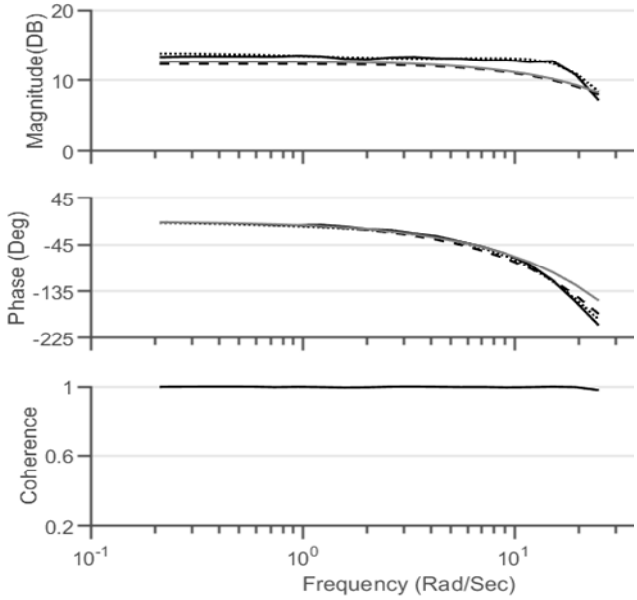

(a)

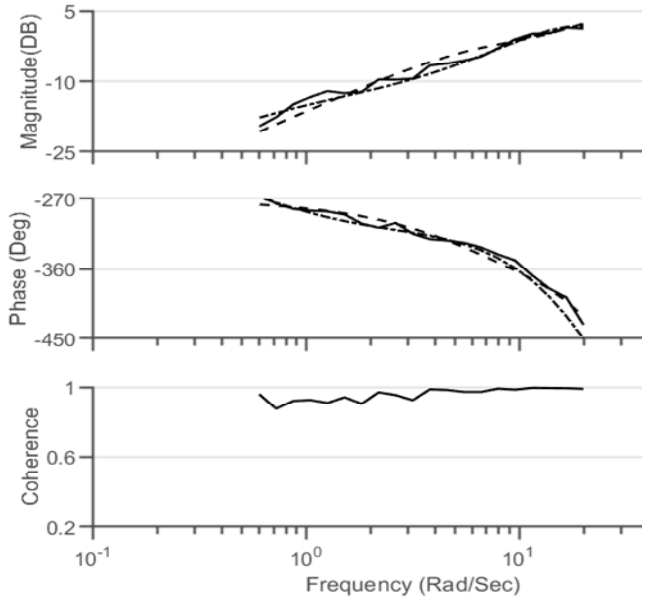

(b)

Figure 6 Frequency domain validation of models, 2.1 m/s on concrete, (a) yaw rate (rad/s) to steering input (μs), $\frac{r}{\delta}$ (jω) (b) roll-rate (rad/s) to steering input (μs), $\frac{p}{\delta}$ (jω) (c) body-axis velocity rate (m/s^2) to steering input (μs), $\frac{\dot{v}}{\delta}$ (jω) (d) lateral acceleration (m/s^2) to steering input (μs), $\frac{a_y}{\delta}$ (jω) (continued)

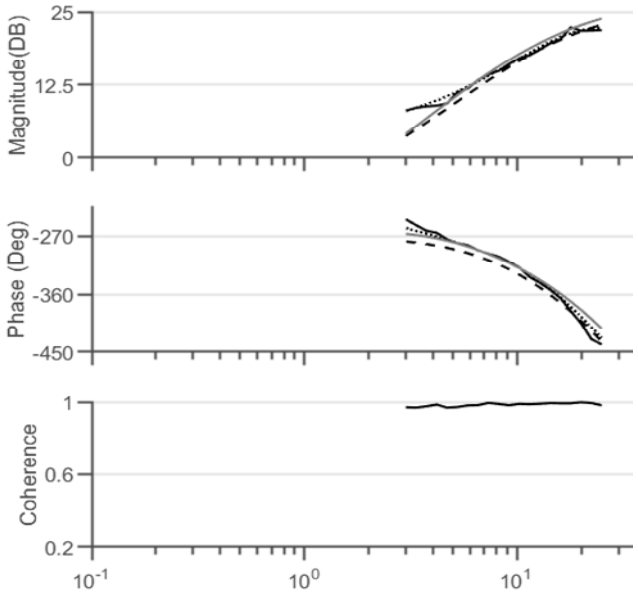

(c)

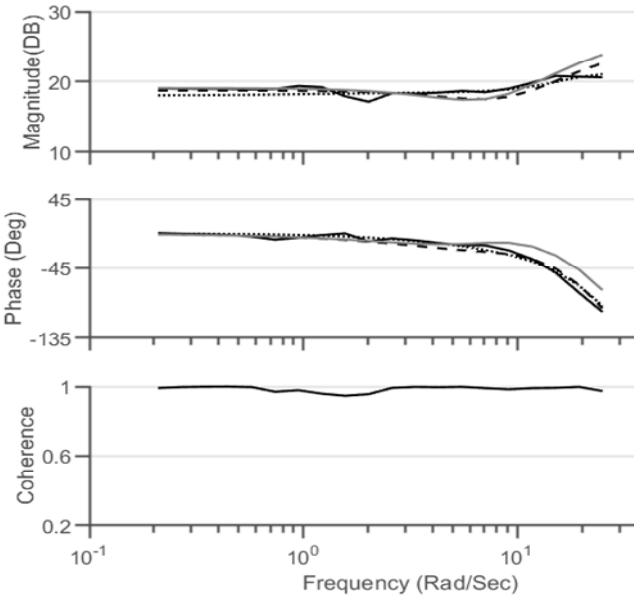

(d)

The equations of motion in state-space form for the roll-yaw model are given in equation (18). The model is based on the derivation in Laws et al. (2006). The integral states $\left(\int \alpha_f \text{ and } \int \alpha_r\right)$ are algebraic states, used to improve clarity of the state-space equation format and reduce complexity of implementation during the system identification process.

$$\begin{bmatrix} 1 & 0 & -h\frac{m_s}{m} & 0 & \frac{C_{\alpha_f}}{m} & \frac{C_{\alpha_r}}{m} \\ 0 & I_{zz} & I_{xz} & 0 & \alpha C_{\alpha_f} & -bC_{\alpha_r} \\ -hm_s & I_{xz} & I_{xx}+m_s h^2 & 0 & 0 & 0 \\ 0 & 0 & 0 & 1 & 0 & 0 \\ 0 & 0 & 0 & 0 & 1 & 0 \\ 0 & 0 & 0 & 0 & 0 & 1 \end{bmatrix} \begin{bmatrix} \dot{V}_y \\ \dot{r} \\ \ddot{\phi} \\ \dot{\phi} \\ \alpha_f \\ \alpha_r \end{bmatrix} =$$

$$\begin{bmatrix} 0 & -V_x & 0 & 0 & 0 & 0 \\ 0 & 0 & 0 & 0 & 0 & 0 \\ 0 & hm_s V_x & -b_\phi & -k_\phi + m_s gh & 0 & 0 \\ 0 & 0 & 1 & 0 & 0 & 0 \\ \frac{1}{V_x} & \frac{a}{V_x} & 0 & 0 & 0 & 0 \\ \frac{1}{V_x} & -\frac{b}{V_x} & 0 & 0 & 0 & 0 \end{bmatrix} \begin{bmatrix} V_y \\ r \\ \dot{\phi} \\ \phi \\ \int \alpha_f \\ \int \alpha_r \end{bmatrix} + \begin{bmatrix} 0 \\ 0 \\ 0 \\ 0 \\ -1 \\ 0 \end{bmatrix} \delta(t-\tau) \quad (18)$$

The states of the model are lateral velocity V_y, yaw rate r, roll rate $\dot{\phi}$, and roll angle ϕ. Algebraic states $\int \alpha_f$ and $\int \alpha_r$ are included for convenience and clarity, as described earlier. The steering angle, δ, is the single input to the model. The other parameters in the model are defined in Table 3.

Table 3 shows the final identified model parameters. As shown in Table 3, some parameters in the model were fixed based on known properties of the vehicle during the test, similarly to the bicycle model. The speed, mass, and front/rear distance to the centre of gravity (a and b) were fixed using the same values as the bicycle model. Because the roll-yaw model has many more parameters, additional parameters were fixed to achieve an identification that had reasonable sensitivity and correlation (Cramer-Rao) between the parameters.

The cross-product of inertia was fixed at zero due to insensitivity and very small resulting identified values, due to the relatively small cross-product of inertia for this vehicle. The mass-moment of inertia for the x-body axis was also fixed to the swing test value, due to poor sensitivity in the model structure. When trying to identify the roll centre location h, the parameter was highly correlated with the suspension spring constant and damping constant, and was fixed based on the observed geometry of the vehicle. The parameters that were identified – the tyre stiffness, x-body axis inertia, spring and damping constants,

and equivalent time delay – were determined with good theoretical accuracy.

The results of the identified suspension spring/damping constants are reasonable values for a vehicle of this size. The equivalent time delay is also reasonable and is consistent with the bicycle model. The values for the mass moment of inertia about the *z*-body axis are within 12% of the swing test value. Additionally, the tyre cornering stiffness of 35.34 N/rad is in the middle of the range (23 N/rad to 55 N/rad) reported from experiments in Hoblet (2003).

The identified mass-moment of inertia and tyre stiffness results for the roll-yaw model are both more consistent with expected values than the bicycle model, indicating better prediction of physical parameters of the model. Additionally, it has a better predictive accuracy as shown by the lower cost functions in Table 5 and Table 6. The model comparisons against the measured data in the frequency domain are shown and discussed later in Figure 6–Figure 7, in comparison with the other two model structures.

Figure 7 Time domain verification, on asphalt at 2.1 m/s

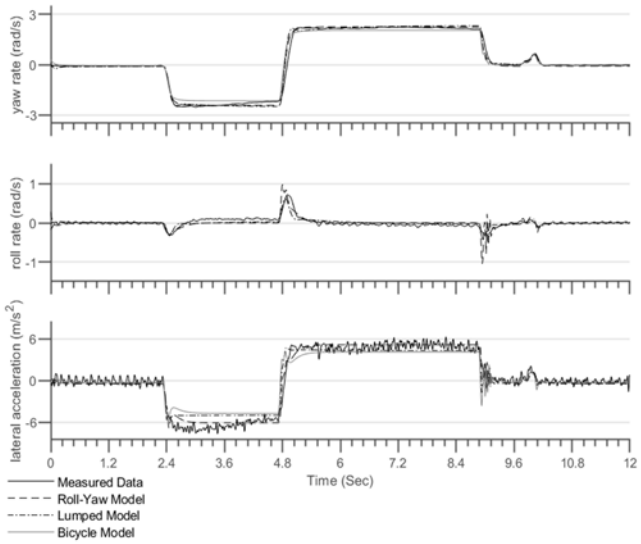

6.3 Lumped model

This model structure is commonly used for aircraft and helicopter dynamic modelling, as described in Ivler and Tischler (2013) and Nelson (1989). The lumped model has lumped Taylor series expansion terms to represent forces and moments in place of the more complex and constrained physical relationships that are present in the previous two model structures. As such, the model includes both roll and yaw dynamics, but in a much simpler form:

$$\begin{bmatrix} \dot{V}_y \\ \ddot{\phi} \\ \dot{r} \\ \dot{\phi} \end{bmatrix} = \begin{bmatrix} Y_v & Y_p & -V_x + Y_r & Y_\phi \\ L_v & L_p & L_r & L_\phi \\ N_v & N_p & N_r & N_\phi \\ 0 & 1 & 0 & 0 \end{bmatrix} \begin{bmatrix} V_y \\ \dot{\phi} \\ r \\ \phi \end{bmatrix} + \begin{bmatrix} Y_\delta \\ L_\delta \\ N_\delta \\ 0 \end{bmatrix} \delta \qquad (19)$$

The notation used is based on the standard aircraft notation from Nelson (1989), where Y is lateral force, L is rolling moment, and N is yawing moment. The states are the same as the roll-yaw model. In this model, each term is individually identified. For example, the combined effect of inertia, tyre stiffness and speed are all lumped into a single identified parameter, $Y_p = \frac{1}{m}\frac{\partial Y}{\partial p}$ which captures the change in specific lateral force (Y / m) as the vehicle undergoes a change in roll rate, p. As another example, N_v represents the change in specific yawing moment, N, with respect to changes lateral speed v, so that $N_v = \frac{1}{I_z}\frac{\partial N}{\partial v}$. Similarly, all the terms (except V_x) represent partial derivatives of the specific forces and moments with respect to the vehicle states. These parameters are not constrained to one another and are identified as independent values, so the physical relationships between the terms are lost, but the model is less constrained and can adapt to fit the data. The $-V_x r$ kinematic term in the lateral velocity rate equation is retained. Unlike an aircraft model, which typically would not include Y_ϕ, L_ϕ and N_ϕ, these stability derivatives have been retained for the rover model to account for the forces and moments generated by the suspension springs, which are largely activated by changes in roll angle.

The results of the identification are shown in Table 4. The physical parameters such as inertia, tyre stiffness, etc., cannot be extracted from the model structure, so there are no physical characteristics for comparison. Still, as shown in Table 4, good insensitivity and reasonable Cramer-Rao bounds for the identified parameters were achieved. Several parameters were set to zero and fixed in the model structure reduction process, as shown in Table 4, because of poor sensitivity and high correlation. Still, the model has several Cramer-Rao bounds that are in the 30% range, due to correlation between the parameters, however, attempts to eliminate any of these terms met with a model that had much poorer fit. As such, these parameters were retained in the model structure at the cost of slightly higher uncertainty in these parameters.

Table 5 DERIVID cost function values (J), 2.1 m/s on asphalt

Response	*Model type*		
	Bicycle	*Roll-yaw*	*Lumped*
r / δ	86.0	51.6	7.69
a_y / δ	66.8	22.1	15.0
$\dot{V}_y$ / δ	99.7	121.5	20.8
p / δ	n/a	58.0	45.1
J_{avg}	84.2	63.3	22.1

Table 6 VERIFY cost values (J) at nominal conditions, 2.1 m/s on asphalt

	Bicycle model	*Roll-yaw model*	*Lumped model*
Cost (J)	0.84	0.40	0.64
TIC	18 %	10 %	17 %

The model costs and plots against the measured data are shown and discussed later, in comparison with the other two model structures, in Table 5 and Table 6, as well as in Figure 6–Figure 7.

7 Predictive accuracy of the model structures in the frequency domain

7.1 Frequency domain model cost

A key measure of the predictive accuracy of the model is the frequency domain cost function, given by equation (11). This cost function quantifies the differences in magnitude and phase of each frequency response, and is minimised in the model identification process. Table 5 provides the associated cost functions for each of the three model types. Lower cost indicates a better fit, where cost values under 100 are considered good, and cost values under 50 are considered excellent. As shown in Table 5, the lumped model has the best cost in the frequency domain, followed by the roll-yaw model, and then the bicycle model. It is interesting that the excellent frequency domain fit for the lumped model, as indicated by the very low average cost of J_{avg} = 22.1 does not translate to better time domain prediction, as shown later, likely due to over-parameterisation of the lumped model and the lack of physical meaning of the identified parameters.

7.2 Frequency response comparison

Figure 6 compares the three parametric models by overlaying each individual response with the measured frequency response. As shown in Figure 6, the bicycle model does not capture the phase as well as the other model structures, resulting in a much higher (worse) cost. Additionally, the roll-yaw model does not capture the yaw rate magnitude in Figure 6(a) as well as the lumped model, also resulting in higher cost shown in Table 5. Due to the constrained nature of the roll-yaw model structure, it was not possible to achieve a better fit. The roll-yaw model and bicycle models do not capture the lateral velocity response as well at low frequency as the lumped model as shown in Figure 6(c), associated with their poorer cost shown in Table 5. In Figure 6(b), the lumped model and roll-yaw model have a similar characteristic and both capture the roll response reasonably well. It can also be seen that the bicycle model curve is missing from this plot, because it cannot capture the roll rate response (no roll-rate state).

8 Time domain verification: predictive accuracy of the model structures

Figure 7 shows the time domain verification results for a doublet manoeuvre performed on asphalt at 2.1 m/s. Note, that this validation data is a different manoeuvre than that used in the frequency domain identification, which was a frequency sweep. The use of a different manoeuvre for verification ensures that the model is not overly tuned to the original data from which it was identified. The resulting cost values are shown in Table 6. Table 6 indicates that the roll-yaw model provided the best predictive accuracy overall as shown in the lower cost and TIC values. The calculation of these cost functions is given by equations (15)–(16). It is recommended that the cost is less than 1–2 and the TIC is less than 35%. Clearly, we have exceeded these guidelines, and it is clear by visual inspection of Figure 7 that the cost values in Table 6 are consistent with acceptable time-domain accuracy of the model. Additionally, the roll-yaw model appears to produce the best predictive accuracy in the time domain, as indicated by the lowest cost. This is consistent with the results in Figure 7, especially in the lateral acceleration response, which is best predicted by the roll-yaw model. The lumped and bicycle models both under predict the acceleration and generally do not capture the character of the response as well, particularly around the transitions at 2.4 s and 4.8 s. However, all three models similarly predict the yaw rate response, although the bicycle model under predicts the peak turn rate response slightly. The roll-yaw model does overpredict the roll response slightly and has lower damping than the true response, as seen at ~9 seconds.

8.1 Robustness to off-nominal conditions

To test the ability of each of the model structures to predict the behaviour in off-nominal conditions, time domain verification was performed for two additional conditions. Verification doublets were collected at two off-nominal cases: artificial grass (as opposed to asphalt) and at a higher velocity of 4 m/s (almost double the identification speed of 2.1 m/s). In the artificial grass case, no changes were made to the model. In the case of the higher speed, the value of V_x was updated to 4 m/s for all models.

The time domain verification cost results for the three models on artificial grass are shown in Table 7, with the corresponding time domain overlay in Figure 8(a). As indicated by Table 7 and Figure 8(a), the roll-yaw model best captured the response on artificial grass, followed by the bicycle model. The lumped model over-predicted the yaw rate and lateral acceleration responses, resulting in the highest cost.

Table 7 Verify cost values (J), at off-nominal conditions

	Artificial grass			*High velocity (4 m/s)*		
	Bicycle model	*Roll-yaw model*	*Lumped model*	*Bicycle model*	*Roll-yaw model*	*Lumped model*
Cost	0.886	0.56	0.810	2.7	1.41	3.3
TIC	22%	19%	24%	18%	15%	45%

The results for the high-speed off-nominal condition showed a similar pattern as the artificial grass case, where the roll-yaw model had the best off-nominal performance, as indicated by the lowest cost in Table 7 and in Figure 8(b). The bicycle model is also able to predict the high-speed response reasonably well, although it overpredicts the yaw rate as compared to the roll-yaw model. The lumped model

is not robust to changes in speed, as shown by the poor cost in Table 7 caused by severely underpredicted responses in Figure 8(b). This is likely because the lumped model only includes speed in the kinematic term and none of the other lumped terms are updated as speed changes.

Figure 8 Verification results at off-nominal conditions, (a) manoeuvre on turf (b) manoeuvre at high speed (4 m/s)

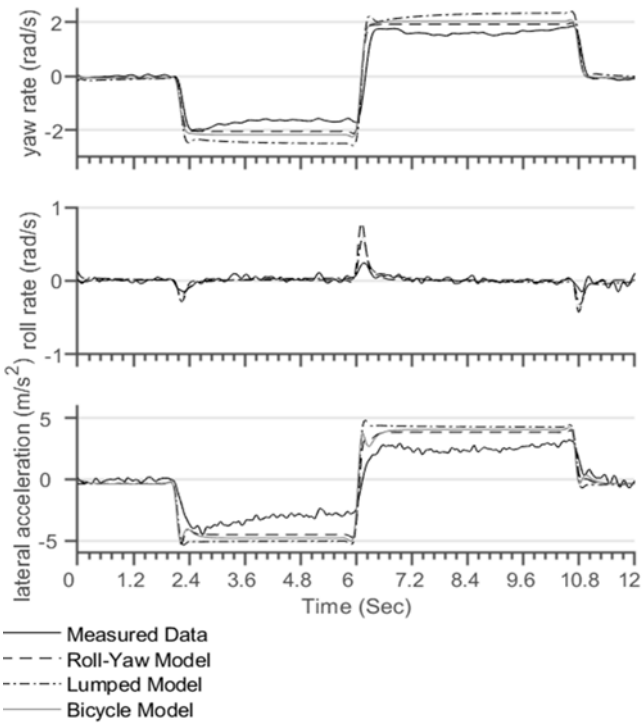

(a)

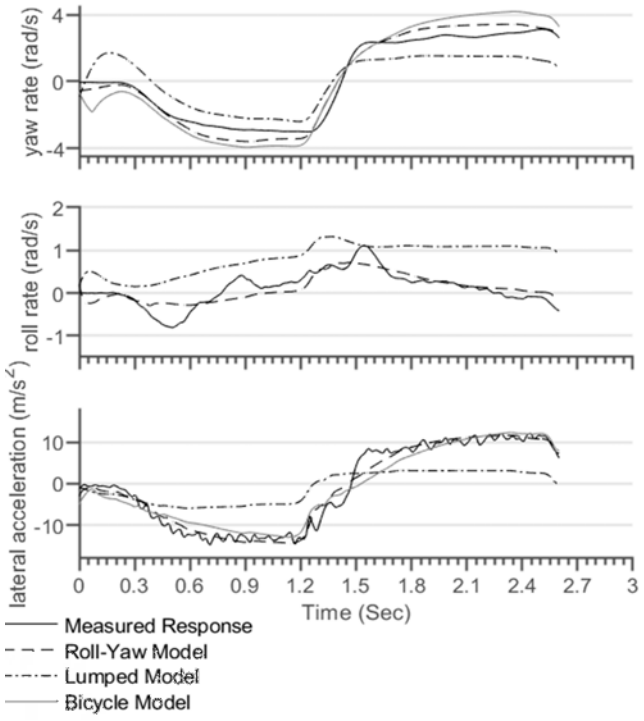

(b)

9 Conclusions

Three different models were identified for a small rover with frequency domain system identification. This work represents the first time these three model structures were directly compared in the frequency and time domain for a small rover, for nominal and off-nominal conditions. Given that these model structures are commonly used to simulate the dynamics of both small and full-scale vehicles, these results are important for understanding the limitations of a model structure that could be used in control system design of an autonomous vehicle. A key conclusion of this work is that the roll-yaw model provides the best overall predictive accuracy for vehicles that change speed and the widest frequency range of accuracy, and therefore is recommended for uses in autonomous control system design. For vehicles that largely operate at a fixed speed, the lumped model structure provides an excellent model that is accurate near the speed of interest but cannot be accurately interpolated to other speeds. The bicycle model is simple, but cannot predict rolling motion coupling and therefore is not recommended for autonomous design. Additionally, the value of frequency domain system identification as a modelling technique was proven. The system identification processes provides a high degree of accuracy in the dynamic response over a wide frequency range, and in the ability to identify unknown parameters such as tyre stiffness coefficients. In future work, the effects of model inaccuracy on a robust steering controller will be evaluated using control design methods that are commonly implemented in the literature, which will provide important guidance on the necessity of system identification and the use of the most accurate model structure.

References

Alcala, E., Puig, V., Quevedo, J., Escobet, T. and Comasolivas, R. (2018) 'Autonomous vehicle control using a kinematic Lyapunov-based technique with LQR-LMI tuning', *Control Engineering Practice*, Vol. 73, pp.1–12, ISSN: 0967-0661, https://doi.org/10.1016/j.conengprac.2017.12.004.

Emami-Naeini, A., Ivler, C.M. and Powell, J.D. (2019) 'Frequency-response and frequency-domain models', in Baillieul, J. and Samad, T. (Eds.): *Encyclopedia of Systems and Control*, Springer, London.

Farag, W. (2020) 'Model-predictive-control complex-path tracking for self-driving cars', *Int. J. Modelling, Identification and Control*, Vol. 34, No. 3, pp.265–277.

Hoblet, P. (2003) *Scale-Model Vehicle Analysis for the Design of a Steering Controller*, May, U.S. Naval Academy, Trident Scholar Report, Anapolis, MD.

Ivler, C. and Tischler, M. (2013) 'Case studies of system identification modeling for flight control design', *Journal of the American Helicopter Society*, January, Vol. 58, No. 1, pp.1–16.

Kang, C., Lee, S. and Chung, C. (2014) 'Comparative evaluation of dynamic and kinematic vehicle models', in *53rd IEEE Conference on Decision and Control*.

Koken, M. (2017) *The Experimental Determination of the Moment of Inertia of a Model Airplane*, in University of Akron Honors Project.

Kong, J., Pfeiffer, M., Schildbach, G. and Borrelli, F. (2015) 'Kinematic and dynamic vehicle models for autonomous driving control design', in *IEEE Intelligent Vehicles Symposium*, Seoul, South Korea.

Laws, S., Gadda, C. and Gerdes, J. (2006) 'Frequency characteristics of vehicle handling: modeling and experimental Validatino of yaw, sideslip, and roll modes to 8 Hz', in *Advanced Vehicle Control, International Symposium*, Hsinchu, Taiwan.

Nelson, R. (1989) *Flight Stability and Automatic Control*, Vol. 2, WCB McGraw Hill, New York.

Petrov, P. and Nashashibi, F. (2014) 'Modeling and nonlinear adaptive control for autonomous vehicle overtaking', *IEEE Transactions on Intelligent Transportation Systems*, Vol. 15, No. 4, pp.1643–1656.

Schildbach, G. and Borrelli, F. (2015) 'Scenario model predictive control for lane change assistance on highways', in *IEEE Intelligent Vehicles Symposium (IV)*, June.

Shao, K., Zheng, J. and Huang, K. (2019) 'Robust active steering control for vehicle rollover prevention', *International Journal of Modelling, Identification and Control*, Vol. 32, No. 1, pp.70–84.

Sinder, J. (2009) *Automatic Steering Methods for Autonomous Automobile Path*, Robotics Institute, Carnegie Mellon University, Pittsburgh, PA.

Tagne, G., Talj, R. and Charara, A. (2013) 'Higher-order sliding mode control for lateral dynamics of autonomous vehicles, with experimental validation', in *IEEE Intelligent Vehicles Symposium (IV)*.

Theodore, C., Tischler, M.B. and Colbourne, J. (2003) 'Rapid frequency domain modeling methods for UAV flight control applications', in *AIAA Atmospheric Flight Mechanics Conference and Exhibit*, Austin, TX, 11–14 August.

Tischler, M. and Remple, R. (2012) *Aircraft and Rotorcraft System Identification: Engineering Methods with Flight Test Examples*, AIAA Education Series, Reston, VA.

Wan, N., Zhang, C. and Vahidi, A. (2019) 'Probabilistic anticipation and control in autonomous car following', *IEEE Transactions on Control Systems Technology*, January, Vol. 27, No. 1, pp.30–38.

Zainal, Z., Rahiman, W. and Baharom, M. (2017) 'Yaw rate and sideslip control using PID controller for double lane changing', *Journal of Telecommunication, Electronic and Computer Engineering (JTEC)*, Vol. 9, Nos. 3–7, pp.99–103.

Zhao, P., Chen, J., Song, Y., Tao, X., Xu, T. and Mei, T. (2012) 'Design of a control system for an autonomous vehicle based on adaptive-PID', *International Journal of Advanced Robotic Systems*, Vol. 9, No. 2, p.44.

Notation

g	Gravity constant, 9.81 m/s^2
m	Mass of vehicle, kg
I	Mass moment of inertia, kg-m^2
δ	Control input steering angle, rad
A	Amplitude of frequency sweep
T_{rec}	Length of frequency sweep record, s
T_{win}	Window length, s
$T(f)$	Frequency response
f	Frequency, Hz
ω	Frequency, rad/s
t	Time, s
G_{xx}, G_{yy}, G_{xy}	Input-autospectra, output-autospectra and cross-spectra
$X(f)$	Input signal, in frequency domain
$Y(f)$	Output signal, in frequency domain
$\boldsymbol{x}$	Array of state-space model states
$\boldsymbol{y}$	Array of state-space model outputs
J	Frequency domain cost function
J_{rms}	Time domain cost function
V_x	Forward velocity, m/s
V_y	Lateral velocity, m/s
β	Sideslip angle, rad
p	Roll rate, rad/s
r	Yaw rate, rad/s
ϕ	Roll angle, rad
ψ	Heading, rad
a_y	Lateral acceleration, m/s^2
C_α	Cornering stiffness, N/rad